Model-independent inversion of x-ray or neutron reflectivity data

Erman Bengu, Monica Salud, and L. D. Marks*

Department of Materials Science and Engineering, Northwestern University, Evanston, Illinois 60208

A technique is described for the model-independent analysis of x-ray or neutron reflectivity data. Rather than trying to find just one optimum solution, the idea is to find the set of solutions that are feasible. The approach is based on inversion of the missing phase information using a feasible set approach coupled with a genetic algorithm search for the set of solutions. It does not require previous knowledge of the chemical constituents or any type of initial model, thus adding a higher degree of objectivity to the analysis. The algorithm is tested on both simulated data and observed data. Issues regarding inversion problems and multisolution algorithms, such as the uniqueness of the solutions, are also briefly discussed.

X-ray or neutron reflectivity is one of the standard techniques for the analysis of surfaces and interfaces. Hitherto, methods available for the analysis of reflectivity data have been limited and vary considerably in efficiency. More on this technique and its application can be found in the reviews by Als-Nielsen,[1] Penfold and Thomas,[2] and Als-Nielsen and Kjaer.[3] The most common approach is a least-squares refinement that starts with boxlike scattering-length-density profile models and that requires a suitable initial model. Note that if the initial model is not close to correct, refinement techniques may converge to the wrong solution. Several model-independent techniques have also been developed and applied with some success, such as maximum entropy,[4,5] simulated annealing,[6] cubic B splines,[7] and parametric B splines.[8] Drawbacks include the computationally intensive nature of some of these techniques and their lack of reliability. In addition, these approaches do not take into account the possibility of multiple solutions, which, as discussed below, is an important issue. Some of these methods have been reviewed in papers by Lovell and Richardson[9] and Lu, Lee, and Thomas.[10] We should also note that the majority of the work in this field is directed toward neutron reflectivity. In part, this is because of the added advantage of changing the contrast using the deuteration of selected layers.[11] In this note, we describe a simple and powerful model-independent method for the fast analysis of x-ray or neutron reflectivity data and the reconstruction of the scattering-length-density (SLD) profile that finds not simply one solution, but a set of feasible solutions that match the experimental data. In essence, rather than relying upon a good guess for the initial model, the method finds the set of feasible models that are consistent with the data. This set can then be used for a subsequent least-squares refinement. This is the same strategy that has been used for many years to solve the crystallographic phase problem (e.g., Ref. 12), and has also been used recently with success to solve surface structures (e.g., Refs. 13–15).

We will focus on x-ray reflectivity, noting that the same algorithm can be used for neutron reflectivity in almost all cases. For cases involving SLD profiles of smaller extent, reflectivity can be treated kinematically.[3] For an infinitely sharp interface, the Fresnel reflectivity (R_F) can be expressed as

$$R_F(Q) = \left| \frac{(Q-Q')}{(Q+Q')} \right|^2, \quad (1)$$

where Q and Q' are the moduli of the scattering vectors in vacuum and in the material, respectively. The measured reflectivity $R(Q)$ is related to the ideal reflectivity $I(Q)$ by

$$I(Q) = R(Q)/R_F(Q) = \left| \int_{-\infty}^{\infty} \frac{d\rho(z)}{dz} \exp(iQz)\, dz \right|^2, \quad (2)$$

where $\rho(z)$ is the SLD profile. Thus, provided that deviations from a kinematical approximation are negligible, x-ray reflectivity is a classical phase problem in one dimension. The basic character of such problems has been extensively discussed in the literature.[16] We have applied a methodology outlined by Combettes[17] (see also Refs. 18–20) to our approach to the phase problem in the case of x-ray reflectivity. The mathematical background for the approach, at least for convex problems, is now quite well understood (see Refs. 17 and 19) albeit mathematically complicated, and it differs in both strategy and concept from more classical methods such as refinements or Lagrangian methods. One of the essential points in this method is to determine all admissible ''*a priori* information'' about the system and exploit it. Such information is used as constraints during the solution by describing it in terms of sets. For x-ray and neutron reflectivity, there are four constraints acting on $\rho(z)$, the charge density as a function of position z:

(i) $\rho(z)$ is positive, (except for a few cases in neutron reflectivity).

(ii) For the medium above the reflecting surface, generally vacuum, the value of $\rho(z)$ is known.

(iii) In the bulk material below the reflecting surface, $\rho(z)$ is also known.

(iv) An upper bound to the value of $\rho(z)$ is usually available.

A common issue in constrained phase determination problems is the uniqueness of the solutions. If the reflectivity problem is of ''compact support,'' i.e., outside of some particular region the derivative $d\rho(z)/dz$ is zero, and this is the only constraint on the problem, it is known that a multiplicity of solutions exist.[16] Even with the additional constraints it is not clear that a unique solution exists for the reflectivity
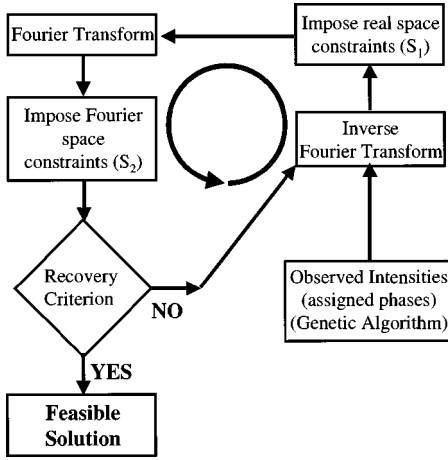
63 195414-1

FIG. 1. Flow chart of the phase retrieval algorithm used for analyzing x-ray reflectivity. The algorithm as a whole involves the projection onto set principles and a genetic algorithm.

problem (i.e., an analytic proof). However, we do know that there will be a set of plausible solutions for $\rho(z)$. If we can find this set, these can then act as the initial models for subsequent final refinement via a least-squares approach. In other words, this set of solutions will act as the initial model input and a degree of objectivity can be imparted to the process, limiting the guesswork and eliminating the issue of uniqueness of the solutions.

The solution method combines two separate algorithms:

(a) The first finds a solution from some initial starting point (some of the phases). For this we used a method of iterative orthogonal projections (see below).

(b) The second is a global search algorithm to find the set of plausible solutions. This is achieved by employing a genetic algorithm.[15]

The first algorithm involves projecting an initial estimate onto two constraint sets; a flow diagram is given in Fig. 1. Given m independent constraints, a feasible solution lies at the intersection of m constraint sets.[17–20] In our case we consider two sets: one in real space, the second in reciprocal space. The first set S_1 consists of all solutions that obey the constraints on $\rho(z)$, a real space object. The second set S_2 is the set of solutions whose moduli are equal to those measured experimentally. These sets can be expressed mathematically as

$$S_1 = \{\rho(z) | \rho(z) \in R^+; \ D_{max} \geq \rho(z) \geq 0; \ \rho(z) = D_{sub},$$

$$z \in \text{substrate}; \ \rho(z) = 0, \ z \in \text{vacuum}\} \quad (3)$$

$$S_2 = \left\{ \rho(z): \ \left| \mathcal{F}\left(\frac{d\rho(z)}{dz}\right) \right|^2 = I_0(Q) \right\}. \quad (4)$$

Here $I_0(Q)$ is the observed ideal reflectivity data as a function of the reciprocal coordinate Q, D_{max} the maximum possible normalized density in the SLD profile, D_{sub} the normalized substrate density, and $\mathcal{F}$ is the Fourier transform. A set is termed *convex* if all points on the line connecting any two

elements of the set are also members of the set. Therefore, S_1 is a convex set while S_2 is a nonconvex set.[17–20] In terms of orthogonal projections, we can construct an iterative method as

$$\rho_n(z) = T^{-1}P_2TP_1\rho_{n-1}, \quad (5)$$

where ρ_n is the current estimate of $\rho(z)$ and ρ_{n-1} is the previous estimate of $\rho(z)$. P_1 and P_2 are relaxed orthogonal projection operators, defined by Eqs. (6) and (7). T is the operator for differentiation and Fourier transformation, and T^{-1} is its inverse. P_1 and P_2 can be expressed by

$$P_1\rho(z) = \begin{cases} 0, & z \in \text{vacuum} \\ \rho(z), & 0 \leq \rho(z) \leq D_{max} \\ (1-\delta_1)\rho(z), & \rho(z) < 0 \\ D_{max} - (\delta_2 - 1)\rho(z), & \rho(z) > D_{max} \\ D_{sub}, & z \in \text{substrate} \end{cases} \quad (6)$$

and

$$P_2T\rho(z) = \sqrt{I_0(Q)} \left[\frac{T\rho(z)}{|T\rho(z)|} \right], \quad (7)$$

where

$$T\rho(z) = \mathcal{F}\left(\frac{d\rho(z)}{dz}\right) \quad (8)$$

and δ_1 and δ_2 are scalar constants (overrelaxation[17–20]) between 1 and 2. P_2 corresponds to the correction of the object at the $(n-1)$th iteration, ρ_{n-1}, with the observed moduli $[=\sqrt{I_0(Q)}]$, and P_1 is the correction for the real-space constraints. For completeness, we have only used orthogonal projections implicitly with a classical Hilbert space L_2 metric; this could be generalized to use Bregman functions and generalized projections.[19]

To implement the algorithm, we start with a guess for the complex structure factors $F_0(Q)$, where

$$F_0(Q) = \sqrt{I_0(Q)} \exp[i\phi(Q)] \quad (9)$$

and $\phi(Q)$ are the unknown phases for which values are sought. It is only necessary to define initial phases for the strongest 10–20 % of measured $I_0(Q)$ values. Using $F_0(Q) = 0$ for the unset values in the first cycle, values for the others are generated automatically at the end of this pass. On any particular guess for the phases, the system of successive orthogonal projections described above (see also Fig. 1) is performed until there is essentially no change in the output. A mathematical figure of merit (FOM) is then calculated as a recovery criterion, defined by

$$\text{FOM} = \frac{\sum |F_n(Q) - F_{n-1}(Q)|^2 + \sum ||F_n(Q)| - \sqrt{I_0(Q)}|^2}{2\sum |F_n(Q)|^2}, \quad (10)$$
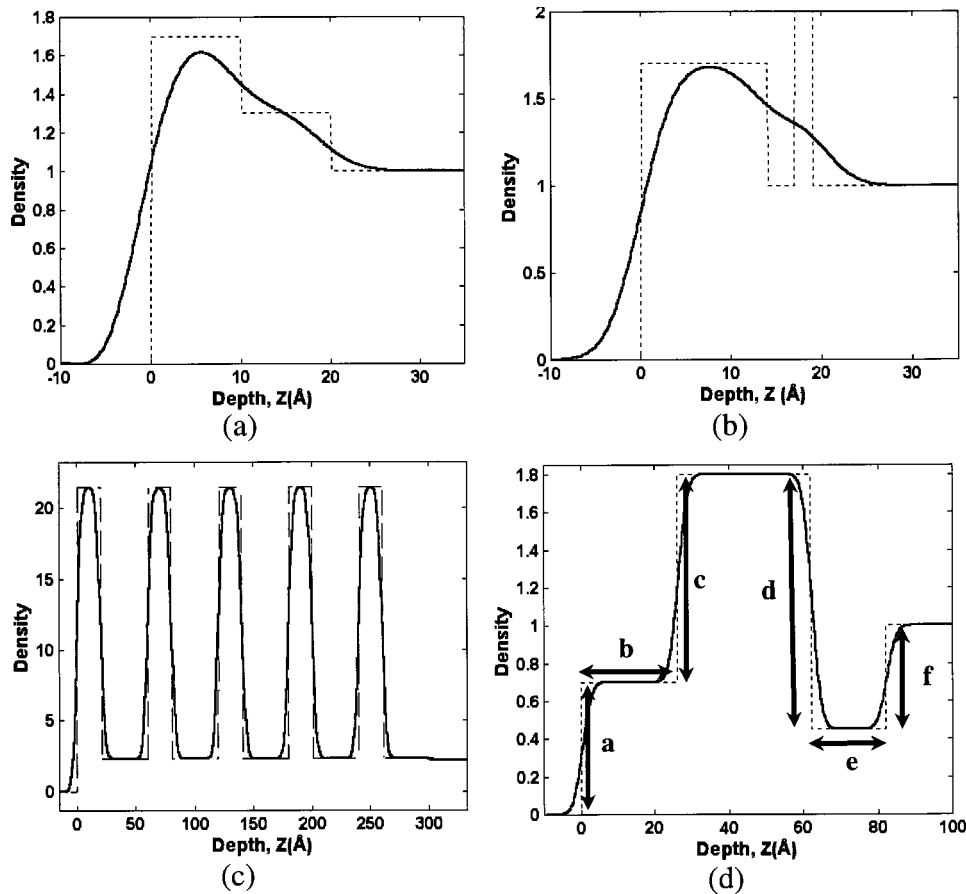
FIG. 2. Test SLD profiles: (a) Two-box model, (b) three-box model, (c) multilayer model, and (d) four-box model. The dotted (or dashed) curves represent the original model, and the full curves indicate models with the roughness applied.

where $F_n(Q)$ and $F_{n-1}(Q)$ are the moduli and phase for the nth and $(n-1)$th iterations, respectively. In the ideal case without noise this FOM is exactly zero for any phase values that satisfy the constraints. However, since the problem is not convex (set S_2 is not convex), there may be many rather different phases that give small to zero values for the FOM. One therefore has to perform a global search to find the set of $\phi(Q)$ values that give small FOM values, this set being the feasible set of solutions for the problem. For this a genetic algorithm (GA) was used to implement a global search to find the best set of phases. Successive projections onto the constraint sets refine the initial phases *locally*, but within the GA a global optimization is achieved by a method similar to ''natural selection,'' which favors phases with better FOM values. Phases with good FOM values are chosen as ''parents'' for the next generation of ''children.'' The output from the algorithm is a solution set in which the solutions are listed in an ascending order with regard to their FOM's. The first solution, or top solution, has the lowest FOM and is considered to be the most plausible solution to the problem. Details on phase restoration using GA's and FOM selection can be found elsewhere in papers by Carmody *et al.*[21] and Marks and Landree.[22] For completeness, we should mention that care and use of sharing algorithms[23] are required to find the set of feasible solutions rather than just one or two solutions.

The approach we are using may at first appear rather complicated and similar to existing methods, but differs from them in several important aspects. First, our use of sets to define the character of constraints and solutions allows a proper, rigorous mathematical formulation of the problem. For instance, recognition that S_2 is nonconvex means that we can unconditionally state that multiple solutions may exist—in other words, there is no guarantee that the reflectivity problem has a unique solution. Second, and more importantly, the approach intrinsically accounts for this possible nonuniqueness. If two (or more) solutions exist, our approach will find them. It is also worth stressing that the algorithm requires *only* three pieces of information: (a) the density of the substrate, (b) an upper limit (which does not need to be very accurate) for the density of the surface material, and (c) an upper bound to the width of the surface material.

No prior assumptions are required regarding the form of the film density, except that it is positive and real. The output will be a set of solutions ranked in terms of how well they match the known information. (These solutions can then be used as the initial models for refinements.) In some cases, particularly with large measurement errors, there may well be several quite different solutions that all match the constraints; in this case, unless some can be excluded on physical grounds, the reflectivity measurements are intrinsically nonunique.

In order to examine the algorithm and solution method, several test models were prepared: (a) a two-box model and (b) a three-box model [Figs. 2(a) and 2(b)], simulating a monolayer of fluorocarbon amphiphilic molecules on water; (c) a multilayer model [Fig. 2(c)], modeled after five alter-
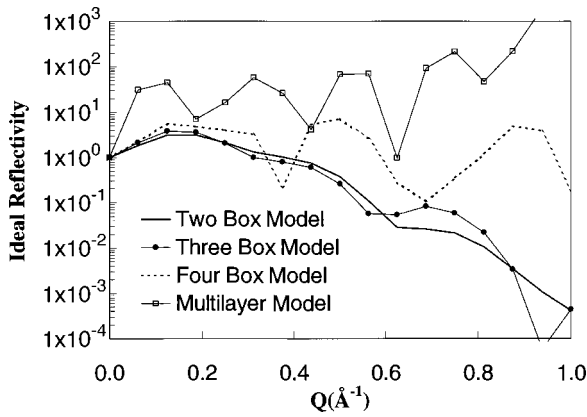
FIG. 3. Simulated ideal reflectivity curves for the models in Fig. 2.

nating layers of Pt and Si on a SiO_2 substrate; and (d) a four-box model [Fig. 2(d)], to scrutinize the uniqueness issue. A Gaussian interface roughness of $\sigma = 3.0\,\text{Å}$ was used for all interfaces in the models. The ideal reflectivity curves for the models were simulated kinematically and are shown in Fig. 3. The algorithm was set to search and reconstruct the phases for the largest 20 or 40 reflections [values of $I_0(Q)$] of a total of 500 (20 for two- and three-box and 40 for four-box and multilayer models). The input consisted of simulated ideal reflectivities, the reciprocal space constraint set S_2, and the real space constraint set S_1. The fundamental challenge in using three- and two-box models is that in the low-Q region ($Q < 0.6\,\text{Å}^{-1}$) the two-box and three-box models do not have significant differences in the ideal reflectivity curves, as shown in Fig. 3. The results, consisting of the top solutions for these cases, given in Figs. 4(a) and 4(b), indicate that the algorithm was able to differentiate between these cases and match the original models very well—nearly exactly, if corrected for the displacements observed (indicated by Δ in the figures). A displacement in real space corresponds to a systematic *phase shift* in reciprocal space with respect to the correct phases, which does not affect the shape of the solution, changing only the relative position of the solution with regard to a reference point. The displacement for the two-box solution is measured to be around 1 Å, while that of the three-box model is approximately 2.5 Å. This insignificant effect can be overcome by implementing stricter real-space constraints in the algorithm; however, we have chosen not to do so for simplicity. Smaller displacements are also observed for the top solutions for multilayer and four-box models, given in Figs. 4(c) and 4(d).

The multilayer model is included to inspect the applicability of the algorithm to the analysis of ultrahard multilayer coatings and similar stratified media. In reality, the reflectivity from such a system is better explained using dynamical modeling[24] due to the effects of multiple scattering between the layers. The top solution for the multilayer model displays
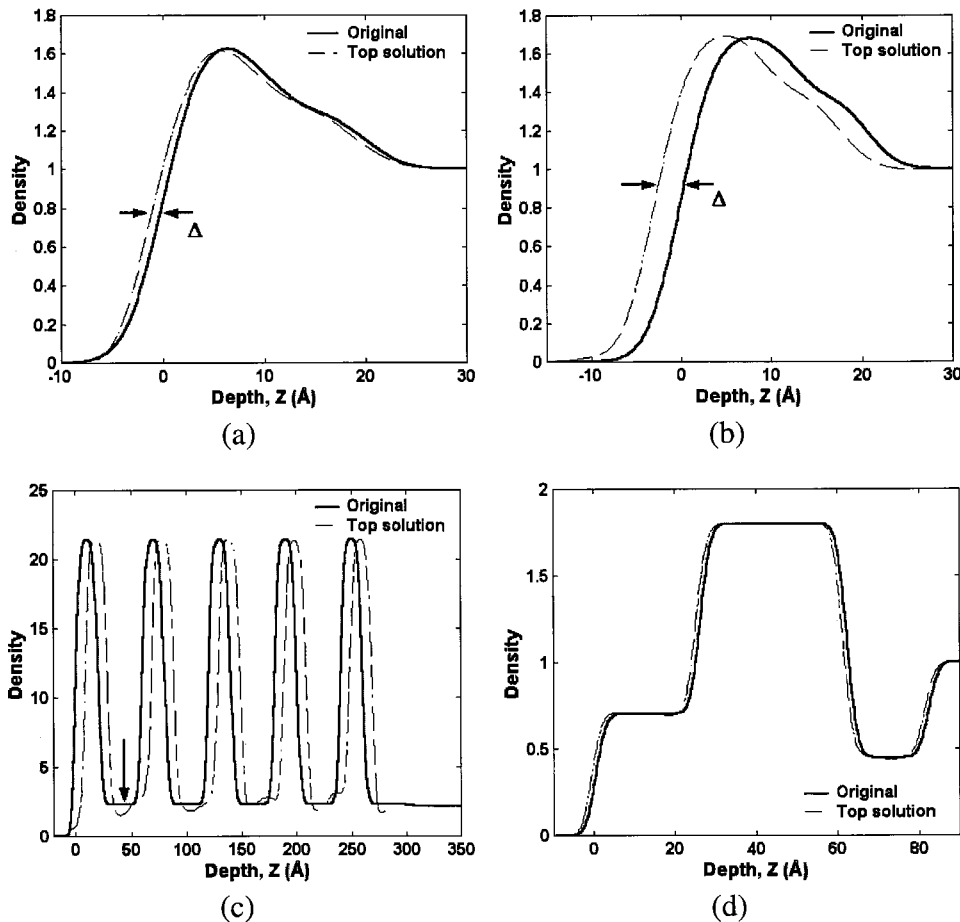

(a)

(b)

(c)

(d)

FIG. 4. Solutions for the test SLD profiles: (a) Two-box model, (b) three-box model, (c) multilayer model, and (d) four-box model. The full curves indicate SLD profiles and the dash-dotted curves represent the solutions found using the present technique. The displacements, indicated by a Δ, in the solutions are discussed in the text. The arrow in (c), the solution for the multilayer model, indicates the deviations in the low-density regions from the original model.

several deviations from the original model, especially in the low-density regions, indicated by an arrow in Fig. 4(c); however, the shape and the width of the high-density layers are correct. This result suggests that to the extent that reflectivity from a multilayer can be approximated kinematically, the solutions from the algorithm can be used as starting points for a least-squares method. This case was also repeated setting phases of the 20 largest values of $I_0(Q)$. Although in general the solutions are very encouraging, the reconstruction of the low-density layers is not as good.

The final simulated case, the four-box model, is used to examine the uniqueness question inherent in both multisolution algorithms and the inversion problem. As shown in Fig. 2(d), several step heights and lengths are nearly identical. Steps $a-f$ and $c-d$ are designed to have no more than a 25% difference between their heights. The same is true of step lengths b and e. Such near-degeneracy of features in the model makes the accurate reconstruction of the step heights and lengths harder, enabling the possibility of structures with a combination of identical features positioned differently to have nearly identical calculated reflectivity curves. The most feasible (top) solution for the four-box case, shown in Fig. 4(d) indicates that the algorithm performed very well. The deviations from the original model are minimal, and all of the features are positioned correctly, thus indicating no apparent signs of problems associated with the uniqueness of the solution.

The ability of this algorithm to obtain a multiplicity of solutions that obey the applied constraints was tested separately on another two-box model. SLD profiles of eight of the top solutions given in a typical trial are compared in Fig. 5(a), where it is clear that a number of plausible solutions with differing features have been reconstructed. For each of these, both a FOM as given in Eq. (10) and a calibration figure of merit (CFOM) that compares the solution phases to those of the original simulation, are calculated. The CFOM and FOM for 250 solutions are plotted in Fig. 5(b). In the CFOM, defined as

$$CFOM = \frac{\sum \{F_n(Q)|1-\cos[\phi_n(Q)-\phi_{n0}(Q)]|\}}{2\sum F_n(Q)},$$

(11)

$\phi_{n0}(Q)$ represents the phase generated by the simulation of the ideal reflectivity curve from a box model and would not be known in an experimental case; however, in examining our algorithm, we use the CFOM as a measure of the suitability of the FOM in determining the fitness of a solution. Two branches of solutions [labeled A and B in Fig. 5(b)] are visible, each of which corresponds to a particular set of similarly shaped solutions as shown in Fig. 5(a). Within a given family, individual solutions differ from each other only subtly and primarily by the aforementioned phase shift, and thus may be treated as a single "quasisolution." In general, it is found from our observations of the two- and three-box SLD profiles generated by our algorithm that the number of quasisolutions in such cases, while greater than one, is small.
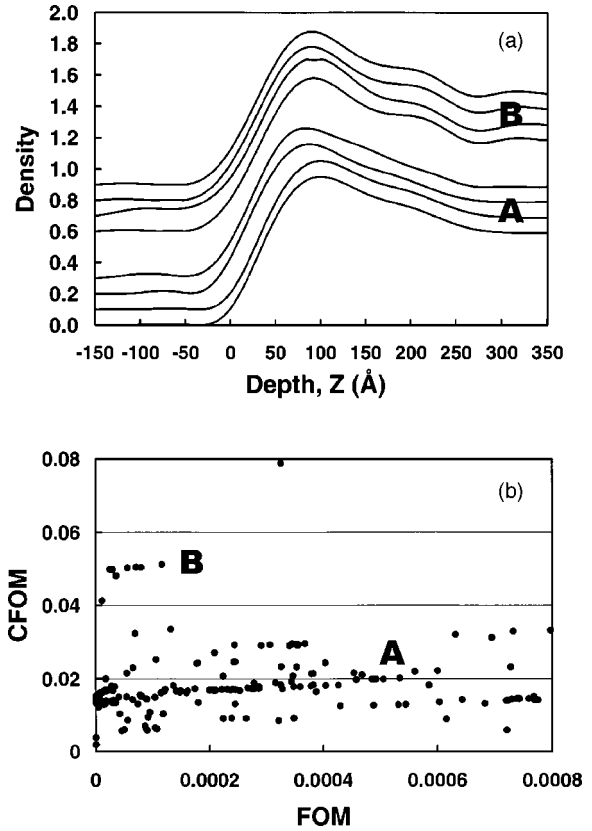

FIG. 5. (a) Multiple solutions generated in a single trial of the algorithm. SLD profiles are displaced along the density axis for clarity. (b) CFOM vs FOM for 250 different solutions.

The final phase of this study consisted of applying the algorithm to the analysis of data from the x-ray reflectivity study of fluorocarbon amphiphile perfluorododecyl aspartate (PFA) monolayers on water by Jacquemain et al.[25] The data consist of four sets, Fig. 6, acquired under the following
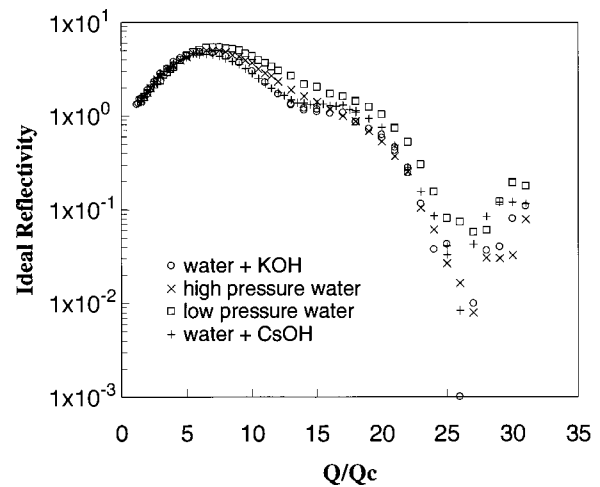

FIG. 6. Experimental data from the x-ray reflectivity study of PFA monolayers on water [by Jacquemain et al. (Ref. 25)]: $\bigcirc$, water+KOH solution, $pH=11.2$, $\pi=30$ mN m^{-1}; $\times$, pure water, $\pi=28$ mN m^{-1}; $\square$, pure water, $\pi=13$ mN m^{-1}; $+$, water+CsOH solution, $pH=11.1$, $\pi=30$ mN m^{-1}.
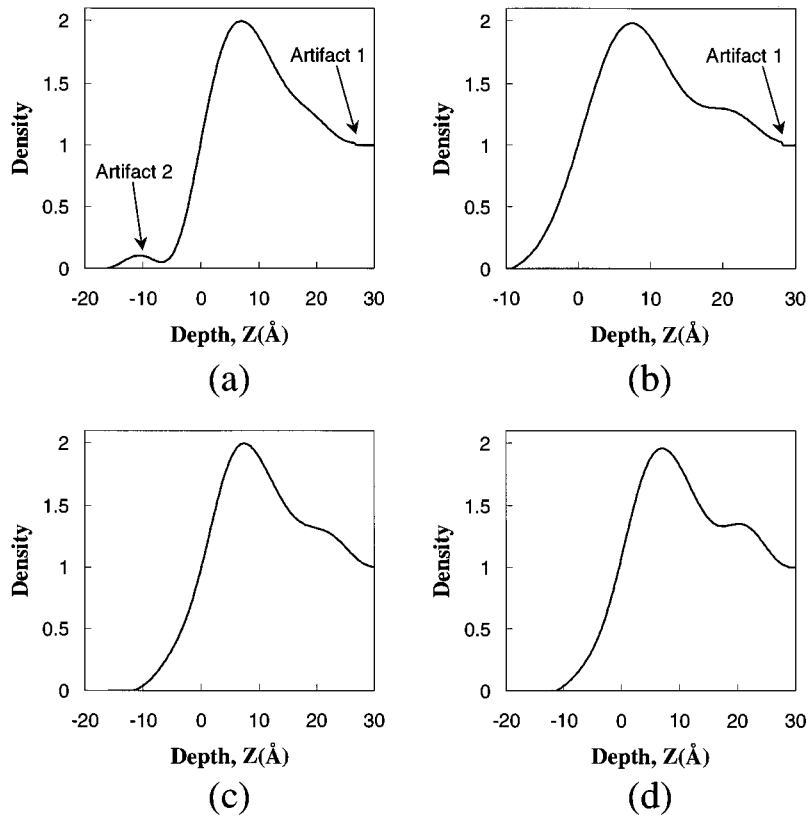
FIG. 7. Solutions using the experimental data for (a) pure water, $\pi = 13$ mN m^{-1}, (b) pure water, $\pi = 28$ mN m^{-1}, (c)water+KOH solution, pH$= 11.2$, $\pi = 30$ mN m^{-1}, (d) water+CsOH solution, pH$= 11.1$, $\pi = 30$ mN m^{-1}.

conditions: (I) pure water, surface pressure $\pi = 13$ mN m^{-1}; (II) pure water, high pressure $\pi = 28$ mN m^{-1}; (III) basic solution (KOH) with pH$= 11.2$, $\pi = 30$ mN m^{-1}; (IV) basic solution (CsOH) with pH$= 11.1$, $\pi = 30$ mN m^{-1}. The original analysis of the data sets from the PFA/water system is given by Jacquemain *et al.*[25] using a least-squares refinement. In addition, Pedersen[7] has also analyzed the same data set using a method involving a profile correlation function. In general, the solutions for the SLD for the PFA/water system from both studies resembles the three-box case examined earlier, although the two-box case is also very similar.

In this analysis, again only the phases of the 20 most intense reflections were varied in the algorithm, although the whole set contained a total of 31 reflections as shown in Fig. 6. The reflectivity values for $Q/Q_c < 1$ in the data sets are greater than unity, probably originating from instrumental resolution or other issues with data acquisition. The top solutions for the data set on pure water are shown in Figs. 7(a) (low pressure) and 7(b) (high pressure). The solution for the low-pressure data set indicates a lower roughness in full agreement with the previous results.[7,25] There is a marked difference between the roughness of the low-pressure solution and the rest of the solutions that are from data sets with much higher surface pressure (~ 30 mN m^{-1}). However, there are two problem areas in the solution as shown in Fig. 7(a) (1) the kink at the PFA-water interface and (2) the hump in the surface region. The cause for these can be a combination of the following, among other possibilities: nonunity beam intensities for $Q/Q_c < 1$ and/or placement of the constraints regarding regions where SLD is zero. Although the top solution for the high-pressure case does indicate the pres-

ence of a similar kink (artifact 1) in Fig. 7(b), the rest of the solutions do not. The head group for the low-pressure solution is visible around 19 Å, which does agree well with the length of the PFA molecule (19.6 Å) calculated previously,[25] allowing for molecular tilt and other effects. The head group for the high-pressure solution, Fig. 7(b), is much more pronounced than that for the low-pressure case, similar to the fit by Jacquemain *et al.*[25] The position for the head group is around 20.5 Å.

The major difference between the high-pressure solution and the solution for the KOH+water case, Fig. 7(c), is the positioning of the extra density for the head group. This feature is around 19.5 Å below the zero reference point for the KOH+water solution. The same feature is found to be further pronounced, and at 21 Å below the surface in the top solution for CsOH+water case shown in Fig. 7(d). The previous values reported by Jacquemain *et al.*[25] and Pedersen[7] agree well with these values.

In summary, a method for the analysis of x-ray reflectivity data has been developed. This method is based on the reconstruction of the missing phase information through methods known both in the image recovery field and in x-ray crystallography. This technique involves application of the feasible sets approach to the retrieval of the missing phases using constraint sets on the real space object (SLD) and the reciprocal space data (ideal reflectivity) coupled with a global search via a genetic algorithm. The method and the algorithm have been tested using four different simulated cases, which resulted in nearly perfect reconstructions of the models in question. Furthermore, the applicability of the technique to the real experimental data has been demonstrated

using experimental x-ray reflectivity studies of PFA on water. The solutions from the method are comparable to those obtained from least-squares fits of molecular model,[25] but without the need to make any initial assumptions about the character of the solution. The same trends in the variation of roughness with the surface pressure of the water, and the positioning of the head groups in the SLD profiles, are observed. For cases where a very good initial model is already known, refinement would be a simpler approach; if this is not the case, and in general to check for uniqueness issues, the model-independent approach outlined herein should be far superior.

*Author to whom correspondence should be addressed.

[1] J. Als-Nielsen, in *Handbook of Synchrotron Radiation*, edited by G. Brown and D. E. Moncton (Elsevier, Amsterdam, 1991), Vol. 3., p. 471.

[2] J. Penfold and R. K. Thomas, J. Phys.: Condens. Matter **2**, 1369 (1990).

[3] J. Als-Nielsen, K. Kjaer, in *Phase Transitions in Soft Condensed Matter*, edited by T. Riste and D. Sherrington (Plenum, New York, 1989), Vol. 3, p. 113.

[4] D. S. Sivia, W. A. Hamilton, and G. S. Smith, Physica B **173**, 121 (1991).

[5] D. S. Sivia, W. A. Hamilton, G. S. Smith, T. P. Rieker, and R. Pynn, J. Appl. Phys. **70**, 732 (1991).

[6] K. Kunz, J. Rieter, A. Gotzelmann, and M. Stamm, Macromolecules **26**, 4316 (1993).

[7] J. S. Pedersen, J. Appl. Crystallogr. **25**, 129 (1992).

[8] N. F. Berk and C. F. Majkrzak, Phys. Rev. B **51**, 11 296 (1995).

[9] M. Lovell and R. M. Richardson, Curr. Opin. Colloid Interface Sci. **4**, 197 (1999).

[10] J. R. Lu, E. M. Lee, and R. K. Thomas, Acta Crystallogr., Sect. A: Found. Crystallogr. **52**, 11 (1996).

[11] S. K. Sinha, Physica B **173**, 25 (1991).

[12] C. Giacovazzo, *Direct Phasing in Crystallography* (Oxford University Press, Oxford, 1998).

[13] L. D. Marks, E. Bengu, C. Collazo-Davila, D. Grozea, E. Landree, C. Leslie, and W. Sinkler, Surf. Rev. Lett. **5**, 1087 (1998).

[14] L. D. Marks, Phys. Rev. B **60**, 2771 (1999).

[15] E. Landree, C. Collazo-Davila, and L. D. Marks, Acta Crystallogr., Sect. B: Struct. Sci. **53**, 916 (1997).

[16] M. V. Klibanov, P. E. Sacks, and A. V. Tikhonravov, Inverse Probl. **11**, 1 (1995).

[17] P. L. Combettes, Adv. Imaging Electron Phys. **95**, 155 (1996).

[18] M. I. Sezan, Ultramicroscopy **40**, 55 (1992).

[19] Y. Censor and S. A. Zenios, *Parallel Optimization Theory, Algorithms and Applications* (Oxford University Press, Oxford, 1997).

[20] L. D. Marks, W. Sinkler, and E. Landree, Acta Crystallogr., Sect. A: Found. Crystallogr. **55**, 601 (1999).

[21] M. Carmody, E. Landree, L. D. Marks, and K. L. Merkle, Physica C **315**, 143 (1999).

[22] L. D. Marks and E. Landree, Acta Crystallogr., Sect. A: Found. Crystallogr. **54**, 296 (1998).

[23] D. E. Goldberg, in *Genetic Algorithms in Search Optimization and Machine Learning* (Addison-Wesley, New York, 1989).

[24] L. G. Parrat, Phys. Rev. Lett. **95**, 359 (1954).

[25] D. Jacquemain, S. Grayer Wolf, F. Levelier, M. Lahav, L. Leiserowitz, M. Deutsch, K. Kjaer, and J. Als-Nielsen, J. Am. Chem. Soc. **112**, 7724 (1990).